Magnetic resonance imaging of convection in laser-polarized xenon

R. W. Mair,[1] C.-H. Tseng,[1,2] G. P. Wong,[1] D. G. Cory,[2] and R. L. Walsworth[1]
[1]*Harvard-Smithsonian Center for Astrophysics, Cambridge, Massachusetts 02138*
[2]*Department of Nuclear Engineering, Massachusetts Institute of Technology, Cambridge, Massachusetts 02139*
(Received 7 October 1999)

We demonstrate nuclear magnetic resonance (NMR) imaging of the flow and diffusion of laser-polarized xenon (^{129}Xe) gas undergoing convection above evaporating laser-polarized liquid xenon. The large xenon NMR signal provided by the laser-polarization technique allows more rapid imaging than one can achieve with thermally polarized gas-liquid systems, permitting shorter time-scale events such as rapid gas flow and gas-liquid dynamics to be observed. Two-dimensional velocity-encoded imaging shows convective gas flow above the evaporating liquid xenon, and also permits the measurement of enhanced gas diffusion near regions of large velocity variation.

PACS number(s): 47.27.Te, 64.70.Fx, 66.10.Cb, 76.60.Pc

I. INTRODUCTION

Two-phase gas-liquid dynamics are important to a wide range of scientific and technical problems, such as the physics of boiling and the engineering of heat transfer systems. To date, however, there are no general methods for mapping the dynamic three-dimensional (3D) properties of complex two-phase flows [1]. As a step toward developing such a method, we demonstrate in this paper nuclear magnetic resonance (NMR) imaging of both gas diffusion and convective flow in a closed two-phase system of laser-polarized xenon (^{129}Xe) gas and liquid, where evaporation of the liquid drives convection of the gas.

NMR is a significant analytical tool for studies of fluid physics. Well established techniques such as magnetic resonance imaging (MRI) permit the mapping of both spin density and the conditional probability of spin displacement over variable time intervals, including measurements of fluid velocity, acceleration, and diffusion [2]. NMR is noninvasive, three-dimensional, and compatible with both transparent and opaque materials [2,3]. In particular, dynamic NMR microscopy can provide images of high spatial and velocity resolution, often reaching the range of 20 μm spatial and 10 μm/s velocity resolution. This technique has been used to study liquids and a wide range of polymer and complex surfactant solutions undergoing flow in a variety of experimental configurations [4–9].

However, applying NMR to two-phase gas-liquid systems poses a significant challenge, because of the small NMR signal provided by gases using the traditional NMR technique of thermal spin polarization in a large magnetic field. For nuclear spins, thermal equilibrium polarizations are approximately 10^{-5} in a magnetic field of a few tesla. Despite this small polarization, NMR can provide excellent sensitivity and image resolution for many applications because of the large spin density of many liquids (e.g., water) [3]. However, conventional NMR is much less effective for gases, and thus for two-phase dynamics, because of the much lower spin density of gases.

Alternatively, laser optical pumping techniques can be used to create large nuclear spin polarizations ($\sim$10%) in dense samples of the spin-$\frac{1}{2}$ isotopes of the noble gases helium (^{3}He) and xenon (^{129}Xe) [10]. Such large polarizations enable high-sensitivity gas-phase NMR, including biomedical imaging of human and animal lungs [11], studies of gas diffusion in porous media [12], and gas-space MRI at low magnetic fields [13]. Furthermore, laser-polarized *liquid* xenon can be created by condensing the laser-polarized gas [14], thus providing a two-phase system in which both the gas and the liquid have extremely high magnetization density. At standard pressure, xenon solidifies at 161 K and melts at 168 K, allowing access to all three phases of xenon at temperatures achieved easily with standard laboratory glassware. It is straightforward to maintain a glass cell containing laser-polarized xenon gas and liquid for lengthy periods ($\sim$20–30 min) in a NMR spectrometer. We recently showed that this liquid permits the acquisition of high-sensitivity NMR spin density images, with the potential for very high resolution micro-images ($\sim 2\ \mu$m) without the need to signal average [15]. Since the xenon liquid NMR resonance is separated by a large 250 ppm downfield shift from the gas-phase resonance, one can use NMR techniques to manipulate or observe either phase selectively.

Several groups have recently used NMR techniques to investigate convection in liquid samples [7,16,17]. Velocity-encoding techniques have been used to compensate for artifacts arising from convection effects in NMR spectroscopy experiments [16], while two groups have visualized liquid convection arising from imposed thermal gradients with two-dimensional velocity images [7,17]. In addition, Brunner *et al.* recently obtained one-dimensional velocity profiles of flowing laser-polarized xenon gas in a pump-driven system [18]. Here, we extend these techniques to a two-phase gas-liquid system. We report two-dimensional NMR velocity images of laser-polarized xenon gas undergoing coherent flow above a droplet of xenon liquid, and demonstrate the utility of this technique to study evaporation, convection, and diffusion in a two-phase system.

II. EXPERIMENT PROCEDURE

The experiment procedure was similar to that described in our recent paper on MRI of laser-polarized liquid xenon [15]. A glass tube of $\sim$25 cm^3 was filled with xenon gas

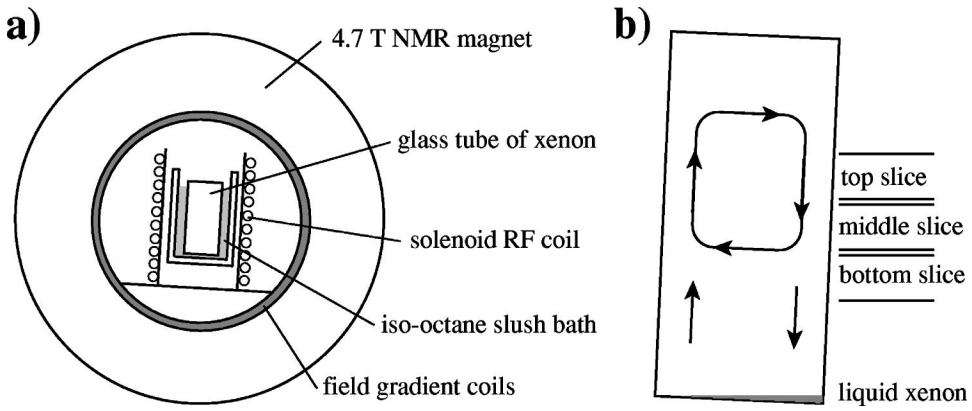

FIG. 1. Schematic of the experimental setup used for the NMR experiments in this paper. (a) shows the arrangement of the glass tube containing the xenon sample, immersed in an iso-octane slush bath in a glass dewar, and placed in an RF coil inside the NMR magnet. This diagram is not to scale. (b) shows a closeup schematic of the tube, indicating the position of the three slices used in two-dimensional imaging experiments, and the likely convective flow pattern indicated by the velocity images of Figs. 4 and 5.

(approximately 3 bar at room temperature) having enriched abundance ($\sim$90%) ^{129}Xe, a small amount of N_2 gas, and rubidium metal. The glass tube was then sealed. While being heated to $\sim$90 °C, the sample was subjected to circularly polarized light at 795 nm from a 15 W diode array laser, resulting in a ^{129}Xe spin polarization of $\sim$5% induced by spin-exchange optical pumping mediated by the rubidium vapor [10]. The bottom of the glass sample cell was then placed in liquid N_2, allowing the xenon to freeze. To help initiate convective gas flow, one side of the tube was then held in liquid N_2 longer to make it colder than the other side. Next, the sample cell was mostly immersed in an iso-octane ice-slush bath in a glass dewar, which maintained the tube bottom at a temperature of $\sim$166 K [19]. The glass dewar, containing the tube of laser-polarized xenon and the iso-octane slush bath, was placed upright in a solenoid RF coil in a horizontal 4.7 T magnet with a clear 20 cm bore. The xenon was observed to melt, forming a droplet of laser-polarized liquid xenon of $\sim$50 mm^3, with xenon vapor (pressure $\sim$1 bar) filling the remainder of the cell. The entire process of xenon freezing and melting required $\sim$1 min, and was performed in the stray field of the 4.7 T magnet (field $>$0.1 T), preserving the large xenon spin polarization [10]. The liquid xenon droplet slowly evaporated over $\sim$20 min, during which time NMR experiments were performed. The limitation to these experiments was usually RF depletion of the enhanced xenon magnetization, rather than the lifetime of the liquid droplet.

All data reported here were obtained using a 4.7 T GE Omega/CSI NMR spectrometer/imager operating at 55.3 MHz for ^{129}Xe, using a homebuilt vertical solenoid NMR coil. The magnetic field gradient coils provided 7 G/cm across the 20 cm bore, which was adequate for the gas-phase diffusion and flow measurements. Single RF pulses monitored the xenon phases in the cell after initial placement in the NMR magnet. A broad spectral peak representing solid xenon was seen initially at $\sim$300 ppm downfield from the gas resonance. As the solid melted, this peak was replaced by narrow lines at 250 and 0 ppm, representing the liquid and gas phases, respectively. Spin density images of the liquid and gas in the cell could be obtained using standard fast gradient echo techniques. These images were similar to those shown in Fig. 1 of Ref. [15]. Generally, however, as soon as the solid had melted, motion-encoded images of the gas-liquid system were acquired. Figure 1 shows a schematic of the laser-polarized xenon gas-liquid sample placed in the NMR instrument, as well as the typical gas-phase convective flow pattern imaged in our experiments (see discussion in Sec. III below).

Spatial information was obtained with a standard spin-warp technique using frequency encoding and (for 2D imaging) phase encoding [2], with data acquisition from gradient echoes formed from inverted readout gradients. Velocity- and diffusion-encoded imaging is usually performed using a spin-echo sequence, with a 180° RF pulse to refocus spin dephasing surrounded by the flow- or diffusion-encoding gradient pulses — a technique popularized by Stejskal and Tanner and known as the pulsed gradient spin echo (PGSE) [20,2]. However, in our experiments, the 180° RF pulse was omitted, since the application of such pulses to laser-polarized samples generally causes large spurious NMR signals, resulting from a combination of RF field inhomogeneity and pulse width missetting [21]. These spurious signals waste the finite, difficult to renew, xenon magnetization created by the laser-polarization process, and also swamp the desired NMR signal which is typically obtained from small flip-angle RF excitations used to conserve the xenon magnetization. A simple modification to the basic PGSE sequence is therefore to remove the 180° RF pulse, and invert the sign of the second gradient pulse, thereby allowing the gradients alone to refocus the dephased xenon spins and produce an echo [21]. Such a technique, known as the pulsed gradient echo (PGE), is susceptible to spatially inhomogeneous (T_2^*) dephasing, unlike spin-echo techniques. However, this is not a limitation in largely homogeneous systems such as that used in the present work.

The NMR echo signal observed in a PGSE or PGE experiment has a Fourier relationship to the probability of spin motion — the so-called displacement propagator, which can be thought of as a spectrum of motion. The echo signal E can thus be written as [2]

$$E(\mathbf{q},\Delta)=\int \overline{P}_s(\mathbf{R},\Delta)\exp[i2\pi\mathbf{q}\cdot(\mathbf{R})]d\mathbf{R}, \qquad (1)$$

where $\overline{P_s}(\mathbf{R},\Delta)$ is the ensemble average displacement propagator, or the probability of a spin having a displacement $\mathbf{R}=\mathbf{r}'-\mathbf{r}$ proceeding from any initial position $\mathbf{r}$ to a final position $\mathbf{r}'$ during the time Δ. $\mathbf{q}$ is the wave vector of the magnetization modulation induced in the spin system by a pulsed magnetic field gradient of strength g and pulse duration δ. The magnitude of $\mathbf{q}$ is $\gamma\delta g/2\pi$, where γ is the spin gyromagnetic ratio. The Fourier transform of E with respect to $\mathbf{q}$, therefore, yields an image of $\overline{P_s}$. When $\overline{P_s}$ is Gaussian, the spins undergoing coherent motion will produce an echo with a relative phase factor $\exp[i2\pi qv\Delta]$, where v is the velocity of the flow; also, the echo will be attenuated by a factor $\exp(-4\pi^2q^2D\Delta)$, where D is the diffusion coefficient describing incoherent random motion (usually self-diffusion) of the spins concerned. In practice, the signal from each pixel in an image is Fourier transformed with respect to q to yield an average propagator, or velocity spectrum, for that pixel's spins. The phase factor accumulated from coherent flow during Δ manifests itself as an offset of the propagator from zero, which in turn yields the average velocity of the spins in that pixel. Applying this analysis to each pixel yields an image in which the signal intensity is indicative of the average local velocity. Similarly, maps of the self-diffusion coefficient D can be produced by fitting the natural log of the measured echo attenuation, $\ln[E(q)/E(0)]$, to $[-\gamma^2\delta^2g^2D(\Delta-\delta/3)]$, the well-known Stejskal-Tanner equation [20].

Two types of NMR experiments were performed. First, we made one-dimensional images (i.e., profiles), along the length of the tube, of xenon gas evaporating from the liquid droplet. To prepare the sample for detection of only *evaporating* gas, a train of selective RF and gradient pulses was used to saturate (i.e., destroy) the laser-polarized gas magnetization, while leaving the liquid phase unperturbed [15]. After a waiting period that varied from 5 to 60 s, velocity profiles were made of the subsequently evaporated polarized gas. Not surprisingly, as the waiting period after saturation increased, the NMR profiles showed that a greater portion of the closed tube was filled by the evaporating gas. The profiles covered a field of view of 150 mm, with 128 acquired points giving a resolution of about 1 mm. For velocity measurements, eight separate profiles, each using different velocity-encoding field gradients, ranging from 0 to 5.5 G/cm, were acquired after the evaporation waiting time. The gradient pulse time δ was 4 ms, while the flow time Δ was 12 ms. Many velocity profiles could be obtained from one sample of polarized liquid xenon, allowing experiments to continue until the polarization of the liquid phase was exhausted. Figure 2(a) shows the sequence of RF and magnetic field gradient pulses used in these 1D NMR experiments, with labels for the separate saturation, velocity-encoding, and imaging portions of the technique.

The second type of NMR experiment was two-dimensional imaging of the steady-state motion of the gas in the closed tube, under the influence of the slowly evaporating liquid xenon droplet. Two-dimensional velocity images were taken of 1 cm thick horizontal slices across the tube axis, without any prior saturation of the gas-phase polarization. Using the gradient echo spin-warp NMR technique [2], 64 different phase-encoding gradients were applied for 2D

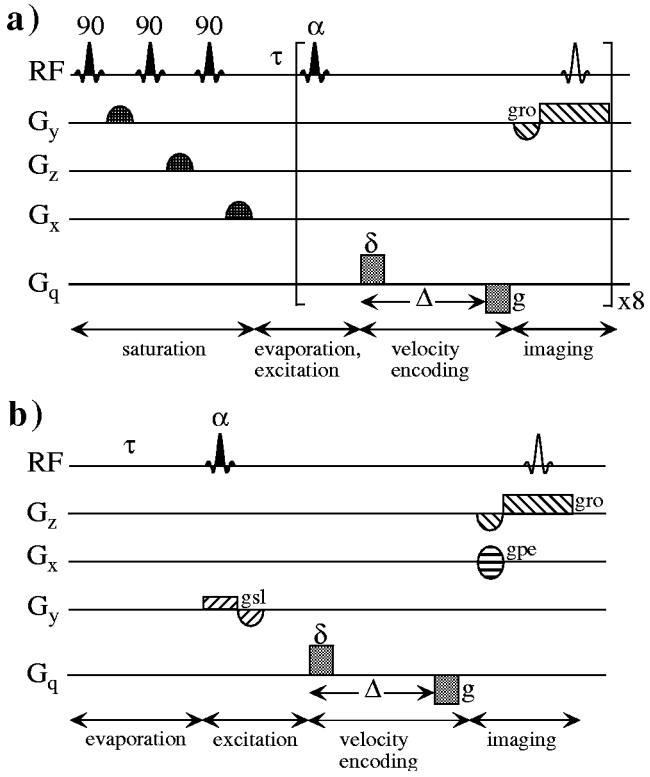

FIG. 2. RF and magnetic field gradient pulse sequences used in dynamic NMR microscopy experiments reported in this paper. The functional sections of these sequences are labeled at the bottom of the diagram. δ and Δ refer to the velocity gradient pulse time and the velocity encoding time, respectively. g, gsl, gpe, and gro refer to the magnitudes of the velocity encoding, slice select, 2D phase encoding and readout gradients, respectively. (a) PGE sequence used to acquire one-dimensional profiles. The sequence begins with a train of saturation pulses, followed by a waiting time τ to allow for evaporation. Eight profiles were then acquired consecutively, with the velocity-encoding gradients (G_q) stepped uniformly for each profile from 0 to 5.5 G/cm along the y (i.e., vertical) axis. (b) PGE sequence used to acquire two-dimensional images. The sequence was repeated 8 times, allowing the velocity-encoding gradients to be stepped from 0 to 5.5 G/cm (y axis) or 5.8 G/cm (z axis). The sequence was also repeated 64 times for each velocity-encoding gradient, allowing the phase gradient to be stepped from negative to positive values, thus permitting a second dimension of spatial encoding. G_q was applied along the y axis for vertical velocity encoding (Fig. 4) or along the z axis for transverse (i.e., within the slice) velocity encoding (Fig. 5).

spatial encoding, giving image data sets consisting of 128 $\times$64 k-space matrices. These were zero-filled to 128$\times$128 across a field of view of 100 mm, giving a final spatial resolution of 780$\times$780 μm. For velocity measurements, eight separate images were acquired, each using different velocity-encoding field gradients, ranging from 0 to 5.8 G/cm. The gradient pulse time δ again was 4 ms, while the flow time Δ was 15 ms, giving the final image a velocity resolution of $\sim$1 mm/s. A delay of 750 ms between each velocity- and phase-encoding step was used, in order for the laser-polarized gas in the slice to be replenished by gas moving in from elsewhere in the tube. Therefore, each velocity image, resulting from 8 velocity and 64 phase encodes, took $\sim$6 min to acquire. The sequence is illustrated in Fig. 2(b). Typi-

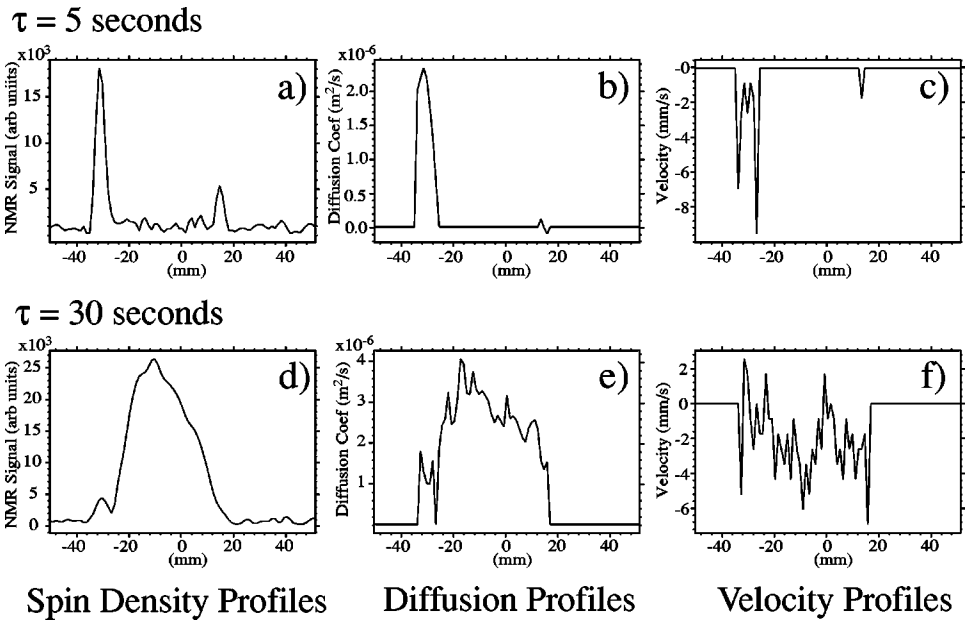

FIG. 3. One-dimensional NMR profiles, along the sample tube's vertical axis, of evaporated laser-polarized xenon gas, acquired using the sequence in Fig. 2(a). Frequency-selective saturation destroyed the initial laser-polarized magnetization from gas in the tube, then profiles were acquired of newly evaporated polarized gas after an evaporation waiting time τ. Profiles (a)–(c) have $\tau=5$ s; profiles (d)–(f) have $\tau=30$ s. (a) and (d) show vertical profiles of laser-polarized ^{129}Xe spin density (in arbitrary units). (b) and (e) show the vertical distribution of the apparent coefficient for xenon gas diffusion along the tube's axis (in $m^2\,s^{-1}$). (c) and (f) show the spatial distribution of coherent velocity of the evaporating xenon gas (in mm/s).

cally, two complete velocity images were obtained from the sample before repolarizaton was necessary. These two images were taken of the same slice along the tube, but with velocity-encoding parallel, and then transverse, to the tube axis. Images of different slices along the tube were obtained after successive repolarization of the xenon.

III. RESULTS AND DISCUSSION

A. One-dimensional profiles

Figure 3 shows typical one-dimensional profiles along the tube's vertical axis of the dynamics of xenon gas evaporation. The top (a)–(c) and bottom (d)–(f) rows show profiles taken at times $\tau=5$ and 30 seconds after saturation of the initial laser-polarized xenon gas, respectively. In all plots in Fig. 3, the abscissa gives the position along the vertical length of the tube, referenced to the approximate center of the tube. Figures 3(a) and 3(d) are spin density profiles, in the absence of motion-encoding gradients. Figures 3(b) and 3(e) are diffusion profiles, giving the coefficient of apparent diffusion along the tube axis for the evaporated xenon gas as a function of position in the tube. Figures 3(c) and 3(f) are velocity profiles, one-dimensional maps of the rate of coherent flow of the evaporating gas along the tube's vertical axis.

The spin density profiles [Figs. 3(a) and 3(d)] show the increase in evaporated laser-polarized xenon gas as a function of time. The growth in the width of the profile indicates the rate at which evaporated xenon moves up the tube. After 5 s, this gas has reached $\sim$1 cm above the liquid droplet, while after 30 s, the evaporated gas has expanded up the tube a distance of $\sim$6 cm. (The smaller peak observed in the 5 s profile at $\sim$15 mm is a signal artifact.) Note that this net flow of laser-polarized gas of $\sim$5 cm in 25 s is more rapid than simple diffusion. For $\sim$1 bar of Xe gas at $\sim$170 K, the xenon gas self-diffusion coefficient is $\sim 2.35\times10^{-6}$ $m^2\,s^{-1}$, giving a one-dimensional diffusion distance of $\sim$1 cm in 25 sec [22].

The axial diffusion profiles in Figs. 3(b) and 3(e) also show an increasing width as a function of time — as with the spin density profiles. After 5 s, the small region filled with evaporated laser-polarized gas exhibits a uniform diffusion coefficient of $\sim(2.0-2.2)\times10^{-6}$ $m^2\,s^{-1}$, approximately the self-diffusion coefficient of xenon gas at 1 bar pressure and 170 K. However, the profile is much less uniform after 30 s, with larger diffusion coefficients observed in the middle of the evaporated gas region. Enhanced self-diffusion (dispersion) can occur where velocity shear or fluctuations exist across one or a few adjacent imaging pixels, i.e., where the coherent flow velocity changes dramatically within a small localized region [6,23]. Such a phenomenon usually occurs only at high differential flow rates, when the effective diffusive motion of the spin is significantly affected as it crosses between streamlines of very different velocity [23]. Thus, Fig. 3(e) suggests that large differential flow rates in the vertical direction exist in this region of the tube.

The two-dimensional velocity images presented in Sec. III B below confirm that large differential gas flow occurs in the sample tube in the form of a single convective roll pattern with gas flowing up one side of the tube and down the other. Velocity shear occurs between these outer regions of high-velocity gas and the slow-moving gas along the central axis of the tube. Thus, very little coherent gas flow is evident in the one-dimensional velocity profile for $\tau=5$ s, shown in Fig. 3(c). In particular, this profile is corrupted by phase artifacts arising from partial volume effects at the edge of the gas cloud. Likewise, for Fig. 3(f) no coherent upward motion

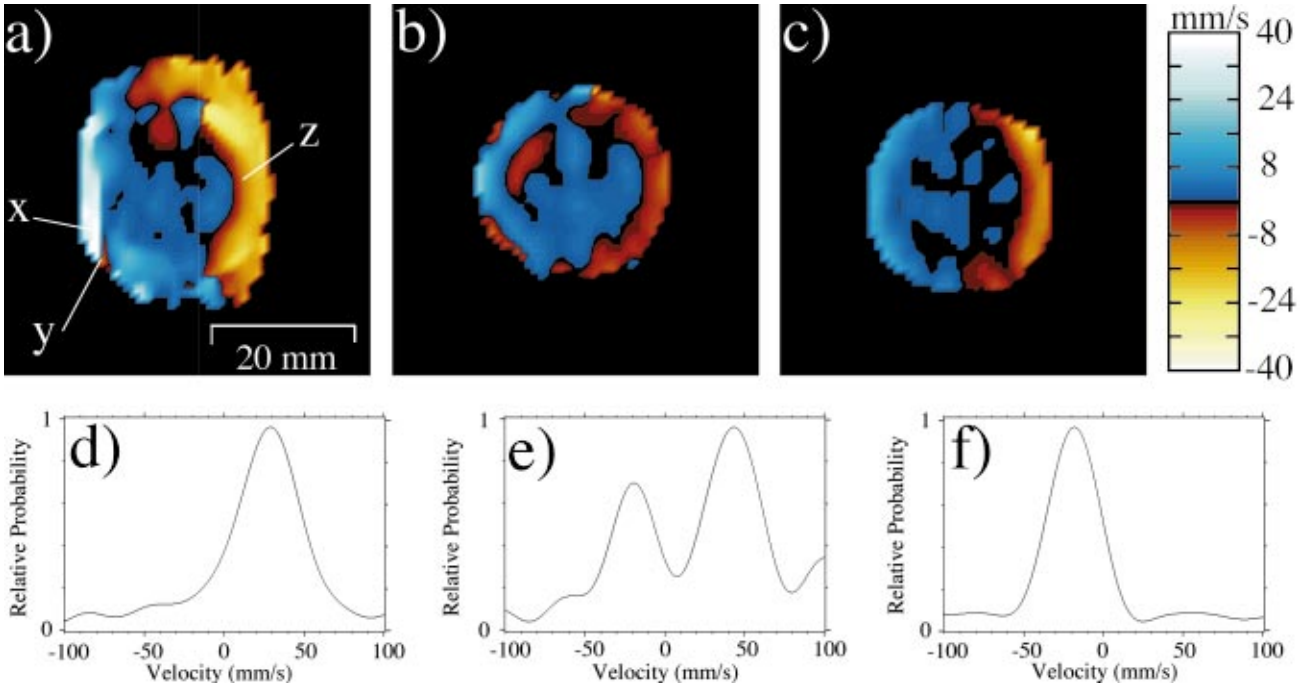

FIG. 4. (Color) NMR vertical velocity images from three 1 cm thick slices of laser-polarized xenon gas undergoing convection above a droplet of liquid xenon. The images were acquired using the pulse sequence in Fig. 2(b), and provide a view looking down on the sample in the cylindrical glass tube. Velocity encoding is for vertical gas flow, i.e., perpendicular to the plane of the page ($G_q = G_y$). The color bar indicates the vertical velocity of the gas in each pixel of the image. (a) Image from a slice nearest the liquid droplet, centered 1 cm below the middle of the tube, showing very high positive and negative gas flow on the left and right sides of the tube, respectively. (b) Image centered at the middle of the tube. (c) Image from a slice 1 cm above the middle of the tube. The three slice positions are indicated in the schematic in Fig. 1. (d)–(f) Sample velocity spectra from pixels *x*, *y*, and *z* in (a).

is observed in the evaporated laser-polarized xenon gas profile above the liquid xenon droplet at $\tau = 30$ s.

B. Two-dimensional velocity and diffusion images

Figures 4–6 provide examples of two-dimensional velocity and diffusion NMR images of laser-polarized xenon gas flow above the evaporating liquid xenon droplet. Figure 4 shows velocity images acquired from three different slice positions along the length of the glass tube, each with vertical flow velocity encoding — i.e., flow parallel to the tube axis, which corresponds to flow perpendicular to the plane of the page. Figure 4(a) is a 1 cm slice above the liquid droplet at $\sim 1-2$ cm below the middle of the tube; Fig. 4(b) is a 1 cm slice in the middle of the tube; while Fig. 4(c) is a 1 cm slice towards the top of the tube, ~ 1 cm above the middle of the tube. The positioning of these slices is shown schematically in Fig. 1(b). Immediately after acquiring the data for each vertical flow image, a second dataset was acquired with transverse flow velocity encoding — i.e., flow orthogonal to the tube. Typical transverse flow velocity images, from the same three slice positions described above, are shown in Fig. 5 with the flow being horizontal in the plane of the page (i.e., left to right). Each pair of images at a given slice position

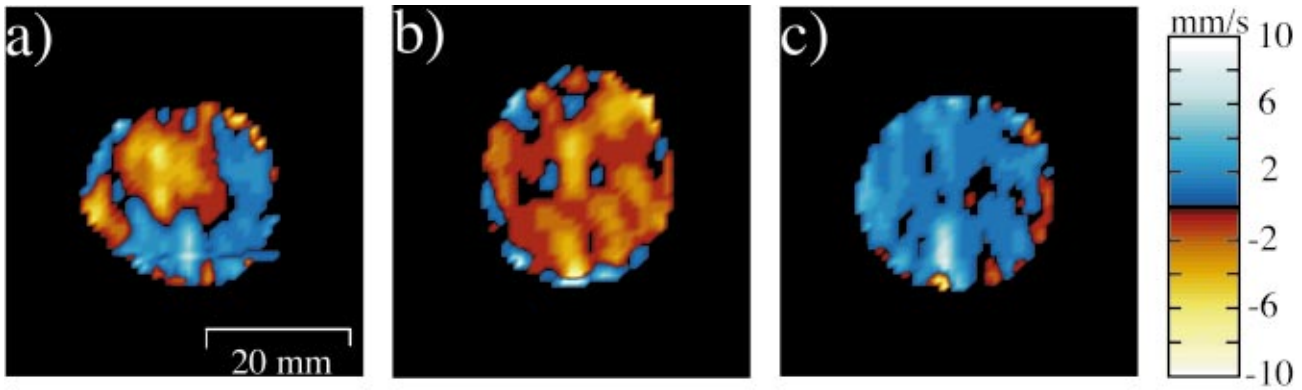

FIG. 5. (Color) NMR transverse velocity images from three 1 cm thick slices of laser-polarized xenon gas undergoing convection above a droplet of liquid xenon. The pulse sequences, slices, and view are the same as in Fig. 4. Velocity encoding is for transverse gas flow, i.e., left and right within the plane of the page ($G_q = G_z$). Each image is acquired immediately after the corresponding vertical velocity image in Fig. 4.

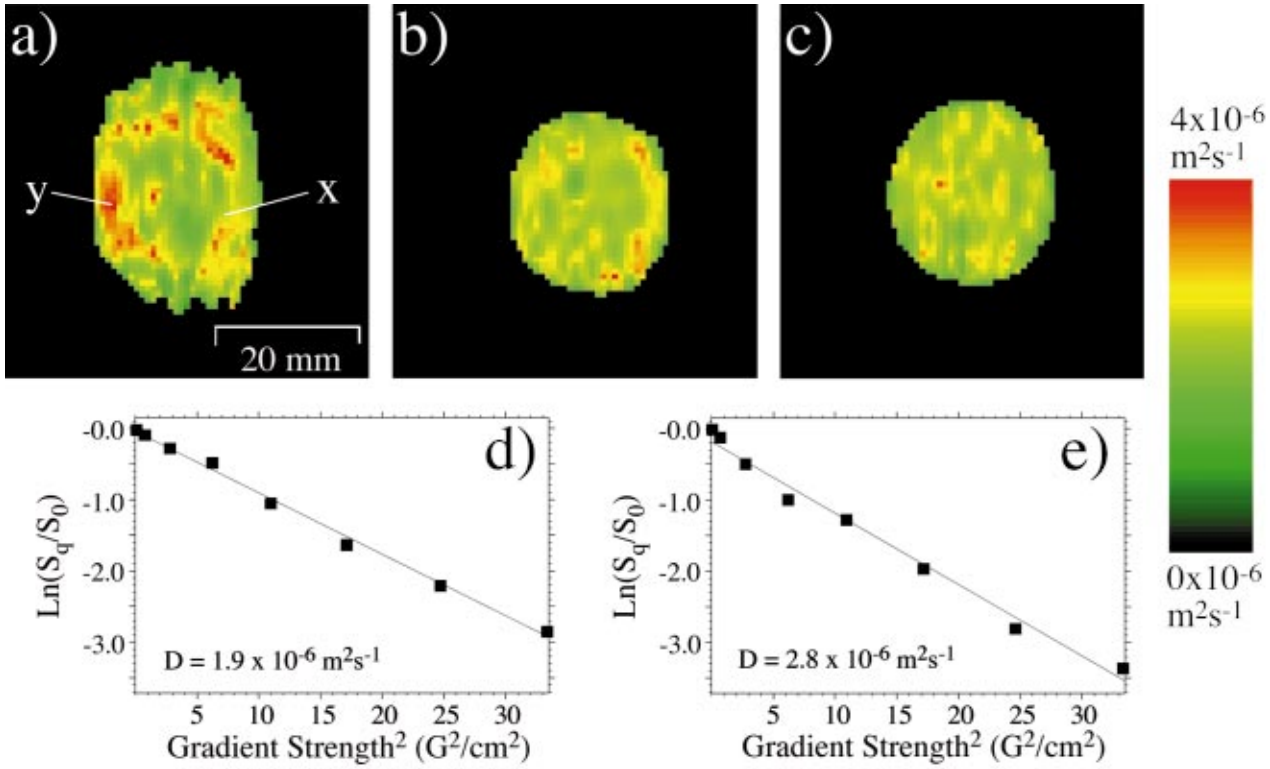

FIG. 6. (Color) NMR diffusion images from 1 cm thick slices of laser-polarized xenon gas undergoing convection above a droplet of liquid xenon. The color bar indicates the apparent one-dimensional self-diffusion coefficient of the gas in each pixel of the image. The images are derived from the same data sets used to produce the velocity images of Figs. 4(a), 4(c), and 5(c). Therefore, (a) has vertical diffusion encoding, in the slice nearest the liquid droplet; (b) has vertical diffusion encoding in the slice nearest the top of the tube; and (c) has transverse diffusion encoding from the same slice nearest the top of the tube. (d)–(e) Examples of signal attenuation plots that yield the spatially localized diffusion coefficient from the slope of the fitted line. Plots in (d) and (e) correspond to pixels labeled *x* and *y*, respectively, in image (a).

[e.g., Figs. 4(a) and 5(a)] were acquired after freshly polarizing the xenon sample. Finally, Fig. 6 shows three diffusion images derived from the same data sets used to generate the velocity images in Figs. 4(a), 4 (c), and 5(c), respectively.

The velocity images in Figs. 4 and 5 clearly show a gas convection pattern in the closed cell, driven by the evaporating liquid xenon droplet and the initial differential temperature of the two sides of the glass tube. In all vertical flow images at the three positions along the tube, a narrow band of gas at the left edge moves upward at high velocity, while on the right edge a narrow band of cooled gas moves downward with high negative velocity. Gas flow velocities near the central tube axis are much smaller. The maximum observed vertical velocities near the tube edges are $\sim\pm 40$ mm/s at the bottom of the tube, ranging to $\sim\pm 20$ mm/s near the top of the tube. Note that at all positions along the tube, the regions of positive and negative vertical gas flow tend to volume average to no net flow, resulting in the near-zero vertical velocity one-dimensional profile shown in Fig. 3(f). The images in Fig. 5 indicate generally slower transverse gas flow than the vertical flow shown in Fig. 4: less than 6 mm/s is typical (positive flow from left to right). The image in Fig. 5(a) is consistent with a lack of transverse coherent flow in this region of high vertical flow rates near the liquid xenon droplet. In the middle of the tube, Fig. 5(b) shows slow coherent flow to the left, while toward the top of the tube, Fig. 5(c) indicates slow flow from left to right. Together, the vertical and transverse velocity images in Figs. 4 and 5 demonstrate a pattern of convective gas flow in the closed glass tube, which is sketched qualitatively in Fig. 1(b).

The images in Fig. 6 show the typically observed spatial variation of the apparent xenon gas diffusion coefficient in the presence of convective flow. The three diffusion images in Figs. 6(a)–6(c) were derived from the data sets used to produce the velocity images shown in Figs. 4(a), 4(c), and 5(c), respectively. For the diffusion images, however, the NMR signal attenuation was fitted to a function of the square of the velocity/diffusion encoding gradient; rather than Fourier transforming the signal with respect to the velocity encoding gradient, as was done to produce the velocity images. The images in Fig. 6 indicate (i) significant spatial variation of the vertical diffusion coefficient in the lower region of the tube, with areas of more rapid diffusion corresponding roughly to areas of larger coherent flow [compare Figs. 4(a) and 6(a)]; and (ii) vertical and transverse diffusion coefficients above the middle of the tube that show little spatial or directional dependence or enhancement. In addition, Figs. 6(d) and 6(e) show the NMR signal attenuation as a function of the diffusion-encoding gradient for the two pixels labeled *x* and *y* in Fig. 6(a), respectively. The plot in Fig. 6(e) displays greater attenuation, as expected from a region with more rapid apparent diffusion.

Finally, we provide the following notes on these demonstrations of two-dimensional velocity and diffusion NMR imaging in laser-polarized xenon.

(1) The observed flow patterns were generally steady during the ~6 min period required to acquire each velocity image. The velocity spectra (i.e., motion propagators) for most image pixels showed a single, well defined velocity peak that indicated coherent, steady xenon gas flow during the image acquisition. Typical examples of velocity spectra are given in Figs. 4(d) and 4(f), which correspond to the pixels labeled *x* and *z* in Fig. 4(a). In a few pixels in regions of the images exhibiting large shear, i.e., large velocity variation over a small distance, the propagator indicated that the flow changed during image acquisition. Figure 4(e) gives an example of such a velocity spectrum, showing bi-directional flow within a single pixel, labeled *y* in Fig. 4(a).

(2) The observed pattern of convective gas flow was fairly reproducible between experimental runs. The experimental procedure involved removing the glass tube from the NMR magnet, repolarizing the xenon at ~90°C, refreezing the xenon, and cooling one side of the tube to re-establish conditions for convective gas flow. The sample was then reinserted in the iso-octane slush bath and placed in the NMR magnet, and letting the xenon melt and form the liquid droplet.

(3) It was necessary to ration the finite laser-polarized xenon magnetization by using low flip angles (i.e., low-power RF pulses) in the imaging sequences. Flip angles $<8°$ were usually used.

(4) Some of the velocity NMR images near the liquid xenon drop suffered from distortion (image stretching) in the phase direction. Figure 4(a) is an example of such distortion. We believe this effect is the result of a time-dependent variation of a background magnetic field gradient arising from the magnetic susceptibility difference between the liquid and gaseous xenon. The effect of such a background gradient was observed in our previous NMR imaging of laser-polarized xenon liquid and vapor [15]. From this past work we estimate that the background gradient at the position of the slice illustrated in Fig. 4(a) is approximately 1 G/cm, and that this gradient varies by about 20% during the course of the experiment, as the droplet begins to evaporate. Such a field variation is about 10% of the applied gradients used for the imaging sequence (1–2 G/cm), which would result in a stretching of the image of ~10% in the phase direction, as observed.

IV. CONCLUSION

In conclusion, we have used dynamic NMR microscopy for quantitative imaging of gas diffusion and convective flow in a closed two-phase system of laser-polarized xenon gas and liquid, where evaporation of the liquid drives convection of the gas. We believe this is the first application of two-dimensional velocity and diffusion NMR imaging to a two-phase gas-liquid system, and one of only a few applications of this technique to quantitative monitoring of heat transfer processes such as convection, rather than the more usual pumped-flow experiments.

Dynamic NMR microscopy yields detailed spatial information on diffusion coefficients and vectorial velocities within a flowing system, as well as the nature of the flow (coherent or turbulent, etc.) through observation of the velocity spectra (i.e., motion propagators) and the echo attenuation for each pixel. However, the lengthy signal averaging and relaxation delays required for such measurements on thermally polarized gas samples restrict the application of dynamic NMR to systems where steady flow can be maintained for lengthy periods (~1–2 h), generally precluding applications to short-lived flow events such as heat transfer processes. The use of laser polarization permits dynamic gas-phase NMR imaging on time scales of minutes, enabling new applications in studies of complex gas-phase and gas-liquid flow.

ACKNOWLEDGMENTS

The authors thank Dr. Sam Patz, Dept. of Radiology, Brigham and Women's Hospital, Boston, MA, for access to the NMR spectrometer on which these experiments were performed. This work was supported by the NSF under Grant No. BES-9612237, by NASA under Grant Nos. NAGW-5025 and NAG5-4920, the Whitaker Foundation, and the Smithsonian Institution Scholarly Studies Program.

[1] M. Ishii, in *Proceedings of the AFERC Conference; Workshop on Two Phase Flow: Phase Change Heat Transfer*, edited by M. H. Kim and B. J. Kim (Pohang Institute of Science and Technology, Pohang, Korea, 1991), Vol., 1, p. 1.

[2] P. T. Callaghan, *Principles of Nuclear Magnetic Resonance Microscopy* (Oxford University Press, Oxford, 1991).

[3] P. G. Morris, *Nuclear Magnetic Resonance Imaging in Medicine and Biology* (Oxford University Press, Oxford, 1986).

[4] Y. Xia and P. T. Callaghan, Macromolecules **24**, 4777 (1991).

[5] S. A. Altobelli, R. C. Givler, and E. Fukushima, J. Rheol. **35**, 721 (1991).

[6] R. W. Mair and P. T. Callaghan, J. Rheol. **41**, 901 (1997).

[7] B. Manz, J. D. Seymour, and P. T. Callaghan, J. Magn. Reson. **125**, 153 (1997).

[8] E. Fukushima, Annu. Rev. Fluid Mech. **31**, 95 (1999).

[9] P. T. Callaghan, Rep. Prog. Phys. **62**, 599 (1999).

[10] ^{3}He can be laser polarized using either of two techniques: spin-exchange optical pumping [see review article: T. G. Walker and W. Happer, Rev. Mod. Phys. **69**, 629 (1997)], or metastability exchange optical pumping [see, e.g., G. Eckert, W. Heil, M. Meyerhoff, E. W. Otten, R. Surkau, M. Werner, M. Leduc, P. J. Nacher, and L. D. Schearer, Nucl. Instrum. Methods Phys. Res. A **320**, 53 (1992)]. ^{129}Xe can be effectively laser polarized using only the first of these techniques. All optical pumping methods have their origin in the work of Kastler and co-workers in the 1950s [see classic review article: W. Happer, Rev. Mod. Phys. **44**, 169 (1972)].

[11] H.-U. Kauczor, R. Surkau, and T. Roberts, Eur. Radiol. **8**, 820 (1998), and references therein.

[12] R. W. Mair, G. P. Wong, D. Hoffmann, M. D. Hürlimann, S. Patz, L. M. Schwartz, and R. L. Walsworth, Phys. Rev. Lett. **83**, 3324 (1999).

[13] C. H. Tseng, G. P. Wong, V. R. Pomeroy, R. W. Mair, D. P. Hinton, D. Hoffmann, R. E. Stoner, F. W. Hersman, D. G.

Cory, and R. L. Walsworth, Phys. Rev. Lett. **81**, 3785 (1998).
[14] K. L. Sauer, R. J. Fitzgerald, and W. Happer, Chem. Phys. Lett. **277**, 153 (1997).
[15] C-H. Tseng, R. W. Mair, G. P. Wong, D. Williamson, D. G. Cory, and R. L. Walsworth, Phys. Rev. E **59**, 1785 (1999).
[16] A. Jerschow and N. Muller, J. Magn. Reson. **125**, 372 (1997).
[17] J. Weis, R. Kimmich, and H.-P. Müller, Magn. Reson. Imaging **14**, 319 (1996).
[18] E. Brunner, M. Haake, L. Kaiser, A. Pines, and J. A. Reimer, J. Magn. Reson. **138**, 155 (1999).
[19] R. E. Rondeau, J. Chem. Eng. Data **10**, 124 (1965).
[20] E. O. Stejskal and J. E. Tanner, J. Chem. Phys. **42**, 288 (1965).
[21] R. W. Mair, D. G. Cory, S. Peled, C-H. Tseng, S. Patz, and R. L. Walsworth, J. Magn. Reson. **135**, 478 (1998).
[22] J. O. Hirschfelder, C. F. Curtiss, and R. B. Bird, *Molecular Theory of Gases and Liquids* (Wiley, New York, 1954), p. 582.
[23] J. D. Seymour and P. T. Callaghan, J. Magn. Reson., Ser. A **122**, 90 (1996).